PROCEEDINGS OF SPIE

SPIEDigitalLibrary.org/conference-proceedings-of-spie

Modeling effects of charge sharing on the response of the FOXSI sounding rockets

Jessie Duncan, P. Athiray, Sophie Musset, Juliana Vievering, Shunsaku Nagasawa, et al.

Jessie Duncan, P. S. Athiray, Sophie Musset, Juliana Vievering, Shunsaku Nagasawa, Juan Camilo Buitrago Casas, Lindsay Glesener, Tadayuki Takahashi, Shin Watanabe, Yixian Zhang, Steven Christe, Alastair MacDowell, Säm Krucker, "Modeling effects of charge sharing on the response of the FOXSI sounding rockets," Proc. SPIE 12191, X-Ray, Optical, and Infrared Detectors for Astronomy X, 121911E (29 August 2022); doi: 10.1117/12.2629443



Event: SPIE Astronomical Telescopes + Instrumentation, 2022, Montréal, Québec, Canada

Modeling Effects of Charge Sharing on the Response of the FOXSI Sounding Rockets

Jessie Duncan^a, P.S. Athiray^{b,c}, Sophie Musset^d, Juliana Vievering^e, Shunsaku Nagasawa^{f,g}, Juan Camilo Buitrago Casas^h, Lindsay Glesener^a, Tadayuki Takahashi^{f,g}, Shin Watanabe^{i,f}, Yixian Zhang^a, Steven Christe^j, Alastair MacDowell^k, and Säm Krucker^{l,h}

^aSchool of Physics & Astronomy, University of Minnesota, Minneapolis, MN, USA

^bNASA Marshall Space Flight Center, Huntsville, AL, USA

^cCenter for Space Plasma and Aeronomic Research, University of Alabama, Huntsville, AL, USA

^dESA, European Space Research and Technology Centre (ESTEC), The Netherlands
^eJohns Hopkins University Applied Physics Laboratory, Laurel, MD, USA
^fKavli Institute for the Physics and Mathematics of the Universe, The University of Tokyo,

Japan

gDepartment of Physics, The University of Tokyo, Japan

hSpace Sciences Laboratory, University of California, Berkeley, CA, USA

iInstitute of Space and Astronautical Science, Kanagawa, Japan

jNASA Goddard Space Flight Center, Greenbelt, MD, USA

kAdvanced Light Source, Lawrence Berkeley National Laboratory, Berkeley, CA, USA

University of Applied Sciences and Arts Northwestern Switzerland, Windisch, Switzerland

ABSTRACT

The Focusing Optics X-ray Solar Imager (FOXSI) sounding rockets are the first solar-dedicated direct-focusing hard X-ray (HXR) instruments. FOXSI rockets use Wolter-1 style HXR optics and solid state double-sided strip detectors. FOXSI images of solar HXR sources are influenced by the point spread function of the optics, the 2D segmentation of the detector into strip intersections, and noise in the detector readout. For FOXSI-4, new high-resolution optics will cause the instrument angular resolution to be limited by the minimum strip pitch of its CdTe detectors (60 μ m).

FOXSI images are also affected by charge sharing in the detector, when one incident photon causes signals in multiple adjacent strips. Charge sharing is more likely the closer a photon is incident to a strip boundary, making it a sub-strip-position-dependent effect. Tests of a FOXSI-3 CdTe detector (with 60 μ m strip pitch) at a synchrotron beamline (the Advanced Light Source) have allowed for characterization of charge shared events. This knowledge is used to develop new methods for achieving sub-strip resolution in FOXSI detectors (0.6-3", depending on incident photon position), applicable in the future to the FOXSI-4 detectors (or other similar systems).

To evaluate the performance of these methods, a model has been developed combining the FOXSI-3 optical and detector response, the latter incorporating lab-measured properties of charge sharing in the system. Using this model, generated sources are convolved with the FOXSI-3 system to simulate FOXSI data. A corresponding deconvolution process then extracts a reconstructed source from the simulated data using the new imaging methods, and the original and reconstructed sources can be compared. We show that the reconstructed source approximates the original with higher spatial resolution than that which results from using strip-based position knowledge only. Notably, we demonstrate a new ability to resolve independent sources located only one strip pitch apart.

Further author information: (Send correspondence to Jessie Duncan)
Jessie Duncan: E-mail: dunca369@umn.edu, Telephone: +1(980) 254-7672

X-Ray, Optical, and Infrared Detectors for Astronomy X, edited by Andrew D. Holland, James Beletic Proc. of SPIE Vol. 12191, 121911E · © 2022 SPIE · 0277-786X · doi: 10.1117/12.2629443

Keywords: Hard X-rays, calibration, the Sun, solar flares, X-ray detectors, solid-state detectors, CdTe, charge sharing

1. INTRODUCTION

Hard X-ray (HXR) observation of the Sun is essential for understanding the dynamics of the solar corona, due to the production of HXRs by both hot (>MK) plasma and non-thermal accelerated particle distributions. Both of these HXR sources are associated with magnetic energy release through reconnection, which powers solar flares.

Many flares appear to follow a "standard flare model" (1), in which particle acceleration occurs near the site of reconnection high in the solar corona, with accelerated populations then traveling down along the legs of flare loops to thermalize in the denser chromosphere. This causes bright non-thermal HXR emission at each loop footpoint, as well as thermal HXR emission along the loop due to evaporation of heated chromospheric plasma into higher layers of the corona.

Fainter non-thermal HXR sources have also been identified in the vicinity of flare loop tops (2). This latter type of non-thermal source is in much greater proximity to the actual reconnection region (and expected acceleration site) than footpoint emission, making it an important diagnostic of flare particle acceleration.

The Reuven Ramaty High Energy Solar Spectroscopic Imager (RHESSI) was a HXR imaging spectrometer which used an indirect Fourier imaging method to investigate flare energy release (3). Given the dynamic range limitations of its indirect imaging method, RHESSI observation of loop-top non-thermal sources occurred largely in events where the brighter footpoints were occulted by the solar limb. Using RHESSI's capability to perform imaging spectroscopy, loop-top non-thermal sources >20 keV were observed to be separated by <5" from nearby thermal sources (emitting at <15 keV) (2).

The Focusing Optics X-ray Solar Imager (FOXSI) sounding rockets are sensitive direct-focusing HXR instruments optimized for solar imaging spectroscopy (4). As a sounding rocket program, the FOXSI rockets function to both make scientific observations during each flight, and also to develop technology for future applications (such as a space-based solar-dedicated instrument using FOXSI heritage). There have been three flights of FOXSI so far, with the instrumentation evolving for every re-flight to increase the performance of the system (4; 5; 6). Further upgrades are underway for the fourth flight (FOXSI-4), which will be the first FOXSI rocket to target observation of a large solar flare via a new "flare campaign" observing strategy (7).

Given the higher dynamic range possible with the use of focusing optics for HXR observation, it is expected that FOXSI-4 (or other FOXSI-heritage instruments) could observe footpoint and coronal sources simultaneously. This dramatically increases the probability of observing loop-top sources, and could also allow for comparison of these two types of non-thermal source in the same event. In the FOXSI rocket energy range (0.5-20 keV)(7), there is significant spectral overlap between observed thermal and non-thermal components of flare spectra, adding an increased motivation to be able to spatially resolve loop-top non-thermal sources from the nearby thermal loop source. Thus, achieving spatial resolution on the order of a few arcseconds will help maximize FOXSI-4 science capabilities.

In Section 1.1, we will discuss how the *FOXSI* instrument spatial resolution can be improved via the development (and evaluation of) new imaging methods. This will improve the capabilities of *FOXSI-4* for flare observations, and also demonstrate imaging methods with the potential to be used in similar segmented detector systems wherever high spatial resolution in the HXR range is needed (such as in future solar-observing space-based HXR instruments).

1.1 FOXSI INSTRUMENTATION

To observe the Sun, FOXSI uses grazing incidence optics paired with segmented semiconductor detectors. FOXSI-3 flew CdTe double-sided strip detectors (8; 9), in which charge generated by the interaction of each incoming photon is read out by orthogonal strip electrodes placed on both sides of the detector. The strip electrodes are in direct contact with the CdTe bulk. On one side, Al electrodes form a Schottky diode structure with the CdTe material, while on the other side Pt electrodes are in Ohmic contact with the wafer (thus, the two sides of these detectors are often denoted the Al-side and the Pt-side). Readout is accomplished with the use of 4 ASICs connected to the detector strip electrodes (64 strips/ASIC, or 128 strips/side).

The FOXSI-3 CdTe detectors have a thickness of 0.75 mm, and a strip pitch of 60 μ m. The incident position of a photon in the 2D detector plane can be located to the intersection between orthogonal strips registering signals, which can function like a pixel in imaging applications (dimensions equal to the square of the strip pitch). At the FOXSI rocket focal length (2 m), the strip pitch corresponds to a \sim 6" angular resolution. This provided similar angular resolution to that achieved with the FOXSI-3 optics (\sim 5").

FOXSI-4 will fly similar CdTe double-sided strip detectors, with the introduction of variable-pitch strips to improve isolation of strip-specific readout electronics (7; 10). The finest-pitch strips will again be spaced 60 µm apart, meaning that the inherent detector spatial resolution will again be \sim 6". However, novel optics development for FOXSI-4 is underway at two different institutions (Marshall Space Flight Center (MSFC) and Nagoya University), with goal optics resolution of 2" and 1" respectively (7). This means that the angular resolution of FOXSI-4 would be detector-limited if the detector resolution remains tied to the pitch of the strips.

Thus we are highly motivated to find methods for extracting sub-strip position information about incident photons in FOXSI-style detectors. In this work, we develop such methods for the FOXSI-3 CdTe detectors, expecting that they will be applicable to the new FOXSI-4 detectors (as well as other similar solid-state detectors with strip-based readout). It is noted that the FOXSI-3 and FOXSI-4 CdTe detectors are different systems, and specific characterization of the FOXSI-4 detectors will additionally be performed before the FOXSI-4 flight to maximize understanding of their performance (10).

A promising phenomena through which we may achieve sub-strip position determination is *charge sharing*, which occurs when a cloud of charge carriers deposited in the detector by a single photon is partially collected by more than one strip electrode on a single side of the detector. The total rate of charge shared events and the *amount* of charge which is shared (the ratio between the collected charge in two adjacent strips participating in a charge shared event) are both expected to be dependent on the sub-strip position of the incident photon (9; 11). This spatial dependence means that if charge sharing behavior can be well understood, observed charge shared event properties can be used to distinguish the response of the detector to incident photons at different sub-strip locations. Therefore, improved event localization can be achieved. Charge sharing in *FOXSI* detectors has been previously used to develop sub-strip source localization with the use of sub-strip-sized pinhole collimators in (9; 11).

The work presented here utilizes results from FOXSI-3 CdTe detector experiments using an X-ray beamline at the Advanced Light Source (ALS), where a sub-strip-sized X-ray beam was scanned across FOXSI-3 detector strips in fine steps. This provides a collection of individual location-specific datasets from ~ 20 different positions within several strips on both sides of the detector, by far the finest-grain characterization of the spatially variable response of FOXSI CdTe detectors achieved to date. New methods for sub-strip source localization have been developed using this new information.

In addition to developing sub-strip imaging methods, it is desirable to evaluate the instrumental performance we can expect after incorporating them. To this end, we have additionally developed a model of the response of FOXSI-3, informed by lab measurements of the FOXSI-3 optics in addition to the knowledge obtained through detector tests. With this model, we can demonstrate the ability of the FOXSI instrument to resolve independent sources located only one strip pitch apart, via charge-sharing-based imaging methods. Additionally, the model is customizable, and can be used in the future with different instrument parameters (e.g. to model the response of FOXSI-4).

In the following sections, we first outline the execution of the FOXSI-3 ALS detector experiments (Section 2). We then show analysis of beam scan data, and use results to develop two new methods for imaging with higher spatial resolution than that of the detector itself (Section 3). Next, we introduce our model of the FOXSI response, including both an overview of how the model is implemented and examples of results using simulated sources (Section 4). Finally, we discuss these results (and some future work needed) in the context of the expected future performance of FOXSI-4 (Section 5). In that concluding section, we also discuss the possibility of incorporation of these methods to improve the capabilities of other future FOXSI-heritage missions.

2. DATA CAPTURE AT THE ADVANCED LIGHT SOURCE

The Advanced Light Source (ALS) at the Lawrence Berkeley National Laboratory is a synchrotron beamline facility (12). ALS beamline 3.3.2* is a general X-ray testing station with an energy range from 4-20 keV, corresponding well to the energy range of the *FOXSI* rockets (for *FOXSI-4*, 0.5-20 keV). We discuss the use of ALS beamline 3.3.2 for *FOXSI* detector tests here in brief, and note that more detailed information is available in (13). The *FOXSI* team proposed for time at the beamline using the ALS RAPIDD proposal process, with help from Dr. Alastair MacDowell, a senior ALS beamline scientist.

At beamline 3.3.2, there is the option of inserting a Si (111) monochromator into the beam path to select a specific photon energy, tunable throughout the stated energy range. The first harmonic of the selected beam energy is suppressed by the monochromator, leaving only the chosen energy and fainter higher-order modes. With the use of movable shutters in two orthogonal directions, the beam can also be reduced to a well-understood rectangular size a few µm in height and width.

In addition to selecting the beam energy and size, the beam position with respect to a target can also be controlled, using a movable stage mounted in the beamline 3.3.2 beam hutch. With a FOXSI detector mounted to the stage, its position can be adjusted and finely controlled in the two dimensions orthogonal to the path of the beam. This allows for the beam to be scanned across the detector in steps of known size (including with step sizes on the order of a few μ m).

2.1 Detector Operation

CdTe detector tests at the ALS were performed using one of the detectors which flew on FOXSI-3 (FEC07), operated at -10 C with 200 V bias applied across the detector bulk. A prototype electronics board (replicating the function of the electronics used in flight) was used to power the detector, apply bias voltage, and carry all communications between the detector and the software used for control and data acquisition. The detector operation and readout is programmable via an included FPGA (for details, see (14)), allowing modification of the detector's low-energy trigger threshold and controlling which strips on each side of the detector are permitted to trigger events. This allows for reduction of troubles with "noisy" strips (which especially occur along detector edges).

During the ALS tests, the detector was operated in a trigger-based read out mode wherein each time a strip registers a signal above the trigger threshold on the Pt-side, a single frame is read out consisting of the current signal in all strips on both sides of the detector. The trigger threshold was set to a value in detector channel units (ADC) corresponding to around 4 keV during the ALS tests. Only the Pt-side of the detector is allowed to trigger due to the fact that it experiences comparatively lower amounts of noise than the Al-side (8). As a genuine event in the detector should deposit similar amounts of energy on both sides of the detector, this is not expected to reduce the utility of the dataset for investigating the Al-side response.

Figure 1 shows the detector testing equipment set up at the ALS, both before and after being mounted to the movable stage. More details about this set-up can be found in (13). Finally, we note that an autoscan procedure was used to automatically collect new *FOXSI* data files at a series of pre-programmed beam positions/energies, with no manual intervention after the scan begins.

2.2 Fine Scan Used for Analysis

The analysis which follows will use a fine, L-shaped detector scan with two orthogonal branches, each with the parameters described in Table 1. This scan first moved in the direction orthogonal to strips on the Pt-side, and then turned to move orthogonal to Al-side strips. In practice, the L-scan was slightly rotated with respect to the detector strip-grid, due to imprecise mounting of the detector. Still, with this scan, we have information at \sim 20 positions within each of eight strips on the Pt-side, and three strips on the Al-side branch of the scan also covered portions of 4 additional strips beyond the fully covered 3. Data from this scan (along with that from other tests at the ALS) is available at the Data Repository for University of Minnesota (15).

^{*}https://als.lbl.gov/beamlines/3-3-2/

[†]The smaller number of strips covered in the Al-side scan was due to two effects: a 40 minute beam outage which occurred during the overnight autoscan, and the fact that a few of the irradiated strips on the Al-side had been disabled due to high noise.

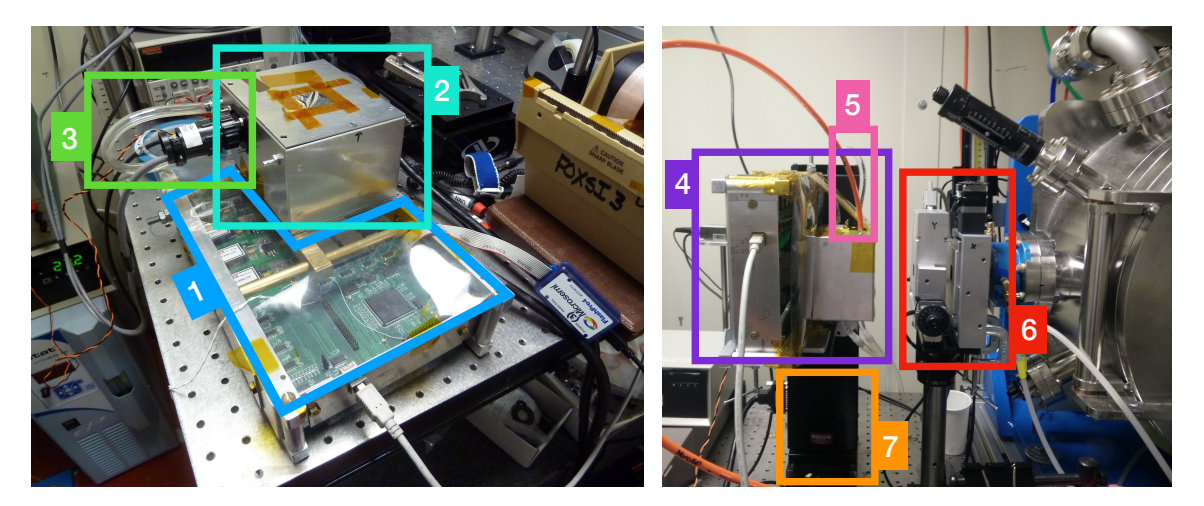


Figure 1. Images of aspects of the FOXSI prototype board testing setup at the ALS beamline 3.3.2 hutch, with key features numbered. Left: 1: The prototype board, viewed from above while set up to test connectivity but not yet mounted to the beam stage. 2: Detector enclosure box (containing detector and thermoelectric cooler (TEC) used to control detector temperature). Flex-circuits connect the detector board to the prototype board below through an aperture that is not visible when they are connected. 3: TEC control cable exits to the left, and chiller water tubes run along the back to remove waste heat. Right: 4: Detector set-up as shown in left image, now mounted on movable stage to be illuminated by the beam. 5: Dry-air purge entering TEC box, to mitigate condensation. 6: Beam aperture (with controllable shutters, to set beam size). 7: Base of movable stage.

3. PURSUING SUB-STRIP RESOLUTION USING ALS RESULTS

We begin this section by defining certain categories of events registered in FOXSI detectors: single-strip, double-strip, and other events. We first define a primary threshold, intended to mimic the trigger threshold of 4 keV (Pt-side: 25 ADC, Al-side: 22 ADC). Additionally, a lower secondary threshold is set at values (Pt-side: 7.3 ADC, Al-side: 7.9 ADC; corresponding to approximately 1.4 keV) above which no significant noise counts were observed in data from non-illuminated detector strips. We apply both of these thresholds during event selection, which categorizes events as follows:

- **Single-strip events** have one strip above the primary threshold on the relevant side of the detector, with every other strip on that side registering below the lower secondary threshold.
- **Double-strip events** have at least one strip above the primary threshold, with one adjacent strip above the secondary threshold (and all other strips on that side below the secondary threshold).
- Other events are all those not fulfilling the single- or double-strip event conditions.

Regardless of method, the event selection for each side is agnostic to the behavior on the other side of the detector (an event may, for example, be single-strip on one side and double-strip on the other).

3.1 Beam Spectra & Energy Selection

To work with scan data in energy space, the locations of the 7 keV X-ray beam and the higher order contributions at 21, 28 keV were used to find a strip-specific gain calibration for all illuminated strips (using a quadratic fit to the ADC-space and energy-space locations of these peaks in the single-strip event spectra).

The resulting spectra at several beam locations are shown in Figure 2. The effects of the primary and secondary thresholds can be observed: the minimum single-strip event energy observed is higher than the minimum energy of double-strip event components. In addition to single-strip (green), double-strip event component energies (red), and all-event spectra (black), Figure 2 also includes the Charge Sharing Addition (CSA) spectra at

Table 1. L-Scan Parameters (Each Branch)

	,	
Beam Size	$2 \mu m \times 2 \mu m$	
Step Size	3 μm	
Scan Length	$540~\mu\mathrm{m}$	
Attenuation	120 μm Al foil	
Integration Time	2 minutes/position	
Approx. Events/Position	4000-5000	
Beam Energies	7 keV (21 keV, 28 keV)	

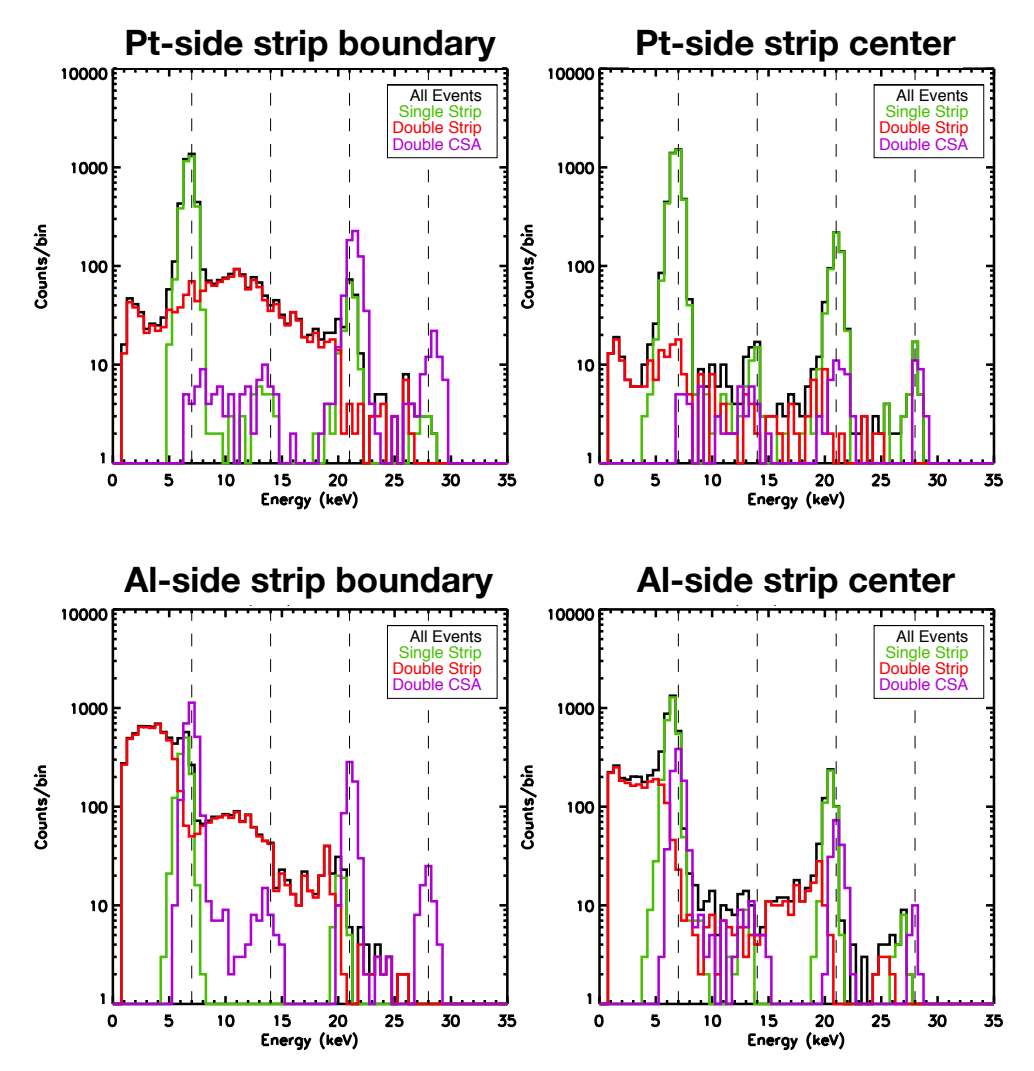


Figure 2. Spectra of the *FOXSI* detector illuminated by a 7 keV X-ray beam (with higher order contributions at 21, 28 keV). Spectra are measured on both the Pt-side (top) and Al-side (bottom) of the detector. **Right:** spectra taken at a position close to the center of a strip on the Pt- (Al-) side of the detector. Single- and double-strip events are shown along with a CSA reconstruction (for each double-strip event, the sum of the two components). **Left:** spectra taken at a beam position close to the boundary between two detector strips. A relatively higher contribution of double-strip events is seen, as the rate of charge shared events increases close to the boundary. The higher-energy lines (21, 28 keV) can be seen to dominantly appear in the CSA spectrum, rather than the single-strip spectrum.

each position, where each double-strip event has had the two component energies summed to approximate the incident photon energy (purple).

The CSA peaks at each beam are located higher in energy than the single-strip peaks, particularly on the Al-side. This is attributed to the loss of a small amount of charge (below the secondary threshold) to adjacent strips in "single-strip" events. Because the CSA peaks are expected to be more accurate, a correction was applied to the gain calibration of Al-side strips to ensure that the CSA peaks were properly located at beam energies. The results of this can be seen in the lower two panels of Figure 2 (Al-side spectra). More details about the gain calibration process can be found in (13).

As a first step in analyzing scan data, we examine the energy-space spectra recorded within a few µm of a strip center (or boundary) on each side of the detector, as estimated in Section 3.2. The energy resolution (estimated by finding the FWHM of peaks in single-strip spectra) was similar to that found for FEC07 in (16) (~1 keV). The locations in which the most (least) charge shared events are expected are the boundaries (centers) of each strip. This expected behavior is confirmed in Figure 2. The spatial dependence of the observed spectra is especially seen in the changing incidence rate of double-strip events between the two positions shown for each side. Near the boundaries, the CSA peaks associated with the higher-energy harmonics (21, 28 keV) represent a larger portion of the observed events at these energies than the single-strip events do on both sides of the detector. For further analysis of charge sharing properties, we will examine the spatial dependence of charge shared event rates in the 21 keV component of the incident beam. To do so, we limit our continued analysis to events where the total recorded energy (energy of a single-strip event, or double-strip CSA energy) is between 17-24 keV.

3.2 Sub-strip Imaging Via Charge Sharing Zones

We now examine the relative number of single-strip, double-strip, and other events within all 17-24 keV events at every beam position. The upper panels in Figure 3 show the total number of single-strip events occurring in each of the strips crossed by each branch of the scan (livetime-corrected single strip count rates at each position). Counts in a particular strip can be seen to rise as the beam enters, peak when the beam reaches strip center, and fall off afterward.

The lower panels of Figure 3 show the percent of the total events in any strip found to be each event type as a function of position. As the beam travels from strip centers (approximately marked by dashed vertical lines) to strip boundaries (approximately marked by solid vertical lines), we see the expected decrease in single-strip events and corresponding rise in double-strip events. The rise in double-strip events associated with each boundary on the Al-side occurs farther into the strip than on the Pt-side, leaving a larger overall zone where these events dominate. This is in line with our expectations, given previous observation of higher charge shared event rates on the Al-side (e.g. 9).

The position of the beam is given in arbitrary coordinates. Strip locations have been estimated by using the position-dependent charge sharing characteristics of the detector. Strip center locations (dashed vertical lines in Figure 3) are estimated by fitting Gaussians to the peaks in number of single-strip events, which are associated with strip centers. Strip boundaries (solid vertical lines in Figure 3) are estimated by fitting Gaussians to the peaks in percentage of double-strip events. The distances from center to center (or boundary to boundary) estimated via these methods are on average within 3% of the strip pitch of 60 µm.

The peaks in the double-strip event fraction near each boundary can also be examined to estimate the size of a "zone" where double-strip events are the most common. The widths of these peaks were taken from the same Gaussian fits, and averaged between the different strips to give typical double-strip event zone widths for each side of the detector. These were found to be $\sim 20~\mu m$, or 33.3% of the strip width on the Pt-side, and $\sim 42~\mu m$, or 70% of the strip width on the Al-side. Additionally, we found the relative percentages of double strip events in total (Al-side: 62%, Pt-side: 33%), calculated over sub-sections of each scan designed to include only full strips.

[‡]By excluding data from portions of the strips illuminated at start/end of each scan (and the data-loss-adjacent segments on the Al-side), we reduce bias which would occur from including intervals where the scans crossed only certain portions of strips. Thus, we closer approximate the total double-strip event percentage that would be observed during a full-detector illumination.

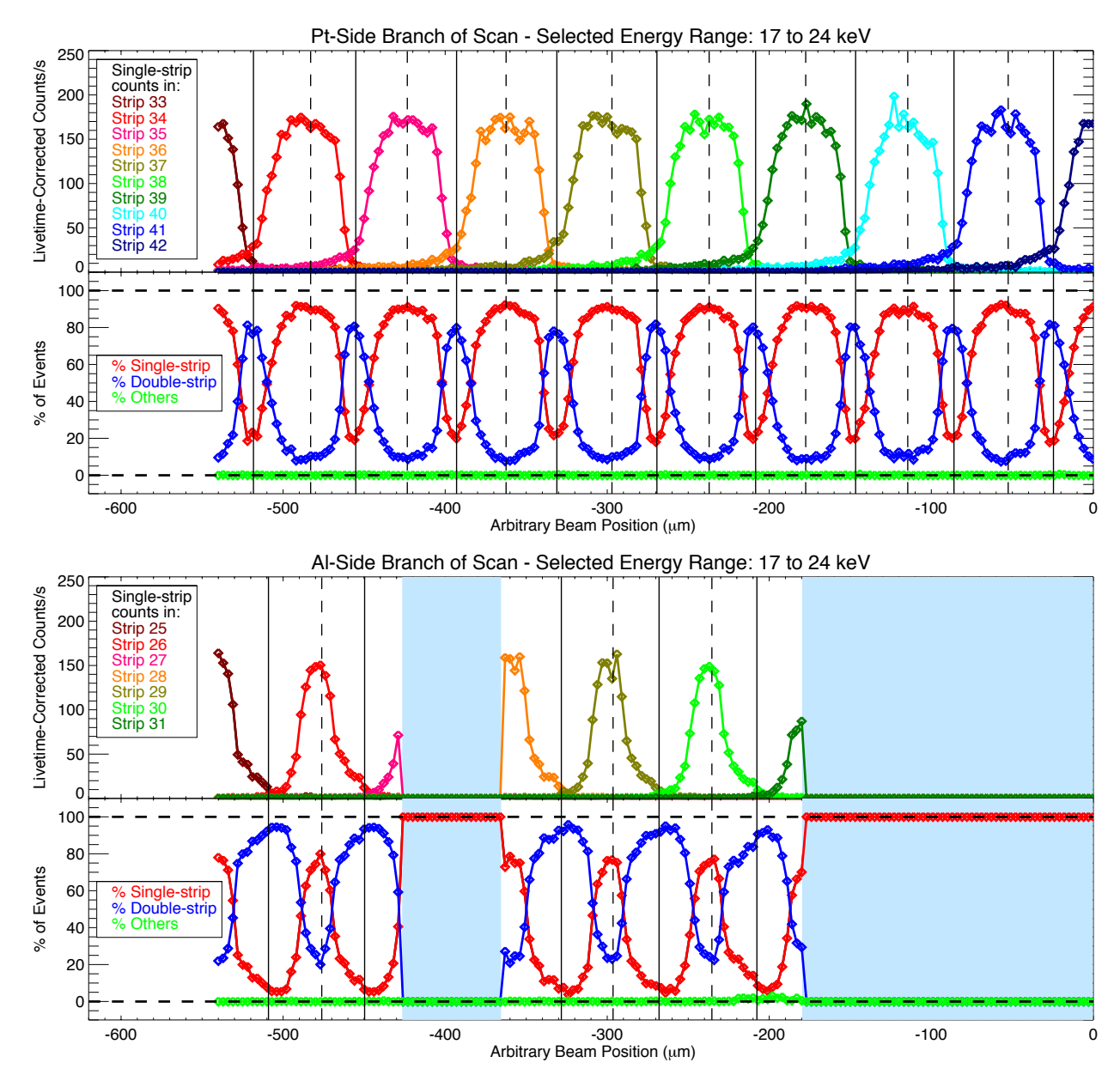


Figure 3. Presentation of recorded event properties in the total-energy range of 17-24 keV during both the Pt-side and Al-side branches of the fine L-shaped beam scan (Pt-side in top two panels, Al-side below). In the upper panel for each side, the livetime-corrected rate of single-strip events in each of the relevant detector strips are plotted as a function of beam position over the course of the scan. In the lower panel for each side, the relative fraction of double- and single-strip events (and other events) are shown at each beam location. In both panels, dashed vertical lines indicate strip centers and solid vertical lines indicate strip boundaries, inferred from the data itself. The blue sections in the lower, Al-side plots indicate a temporary overnight beam shut-off (left) and the beam's passage across several disabled strips (right).

Division of a strip-intersection into sub-strip-sized zones

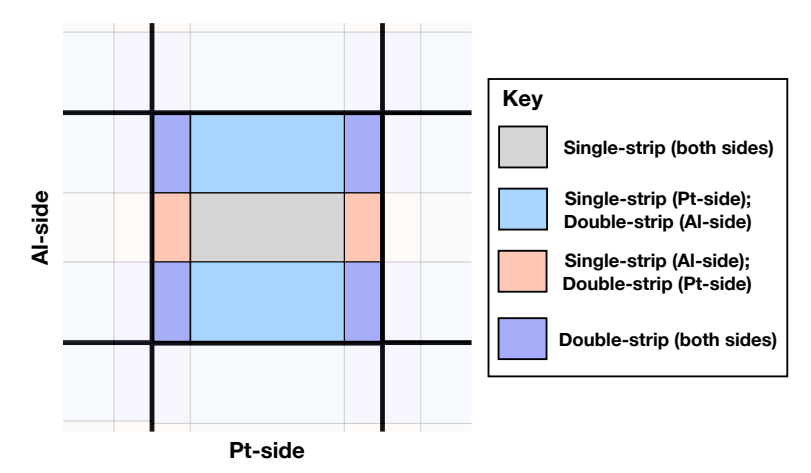


Figure 4. Visual representation of sub-strip zones used in a coarse increased-resolution imaging method. Key describes what type of event is most likely to be recorded when a photon is incident on each of the zones.

The total percentage of events which are double-strip was found previously in (9), using a Am-241 radioactive source to illuminate the detector. They found the following percent of events to be double-strip: at 18 keV, Al-side: 40.8%, Pt-side: 22.1%, at 60 keV, Al-side: 58.4%, Pt-side: 57.2%.

3.2.1 Implementing Zone-Based Imaging

With a geometric understanding of where double-strip events are most likely to occur, it is possible to implement a method for coarse sub-strip imaging. Using the double-strip event zone widths, each strip intersection is divided into nine zones according to whether single- or double-strip events are more likely on each side of the detector. Figure 4 shows these zones within one strip intersection.

We will call this new method *zone-based imaging*. In zone-based imaging, we assign each event to one of the sub-strip zones, rather than to an entire strip intersection. Figure 5 shows the conventional (top) and new, zone-based (middle) methods of generating images of the emission recorded at two different beam positions: one near the center of both the Pt-side and Al-side strips, and one near the boundaries.

To compare the performance of this method to that of the conventional strip-based imaging method, we find it instructive to consider the effective "pitch" of the zones to which events can be located, defined here as the distance between two adjacent zone centers. There are several different pitches due to the different zone sizes, but we note that the greatest of them is a bit less than half the size of the original strip pitch (\sim 25 µm, or \sim 2.6" at the FOXSI). Thus, regardless of incident photon location within a given strip, this method has at least improved the spatial resolution of the detector by a factor of two over that of the conventional strip-based imaging method.

3.3 Sub-strip Imaging Via Energy Ratios

The method of Section 3.2 already represents a significant achievement in utilizing charge sharing behavior to improve the resolution of the FOXSI detectors. However, it does not yet take advantage of all of the information charge sharing provides; further information about the position of the incident photon is encoded in the relative magnitudes of the two energies recorded in a double strip event, with a more even energy split indicating an event closer to the boundary. Energy information in charge-shared events was previously demonstrated as a tool for further sub-strip resolution in a FOXSI CdTe detector in (11). In that work, the incident photon position, X, for each event was estimated using the expression[§],

^{§(11)} has a typo in this expression where it is defined in their Figure 12. This is confirmed to be the correct expression (Shunsaku Nagasawa, personal communication).

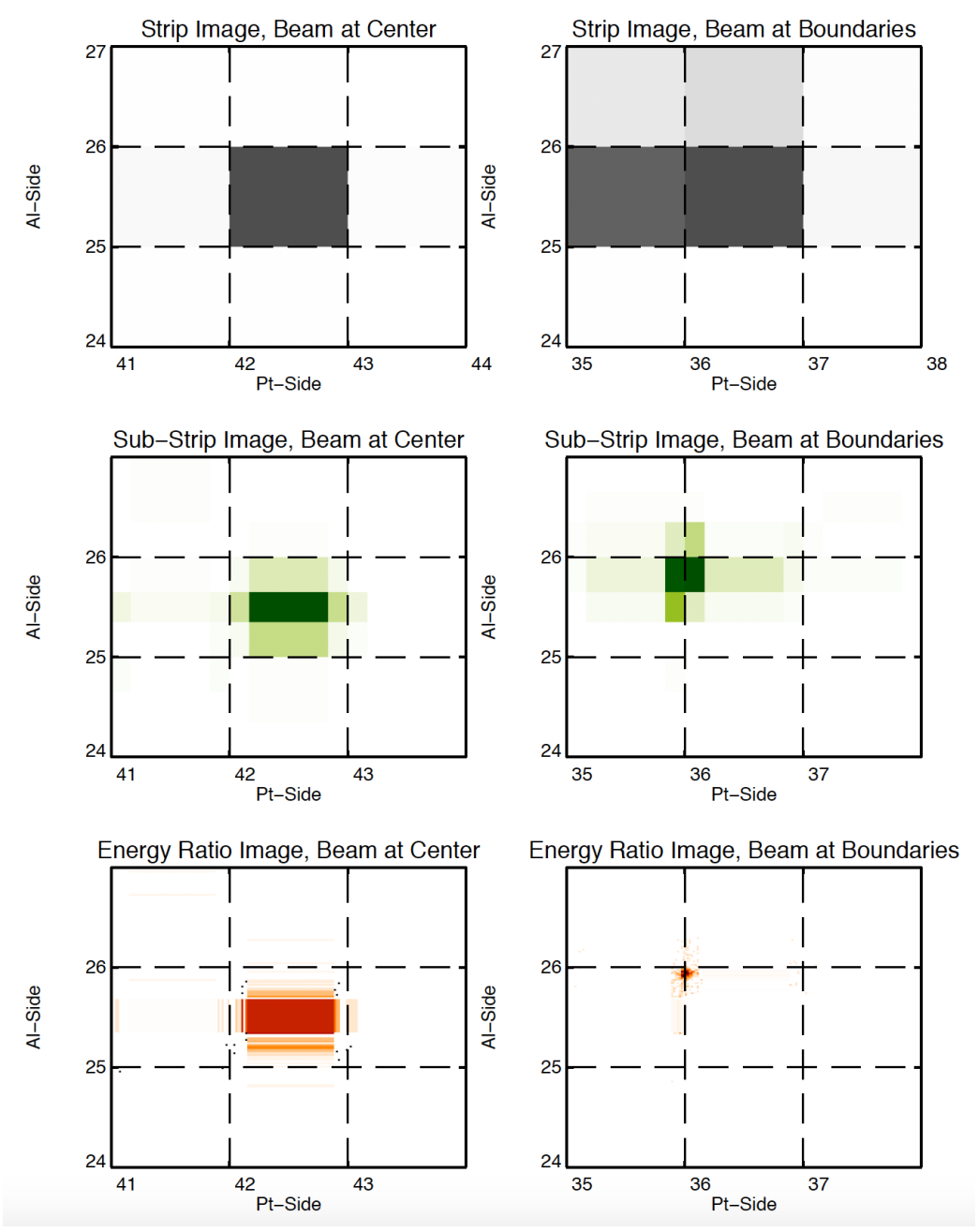


Figure 5. Six example images of a 2 μ m \times 2 μ m beam illuminating the *FOXSI* detector (Left: beam near centers of strips on both sides of the detector, Right: beam near boundaries of strips on both sides). Each image shows a very small section of the detector (three strip widths wide in each direction), with dashed lines indicating strip boundaries. In the top two panels imaging is done via the traditional method, where each photon is located to the two strips (Pt-side, Al-side) which registered the maximum energy. In the middle two panels, each photon has instead been located to a sub-strip zone (see Figure 4) using charge sharing rules defined in Section 3.2. Improvement in beam localization is seen in both cases. In the bottom two panels, imaging is done via the method described in Section 3.3, in which the ratios between energies in the two strips are used to further refine the estimated position in double-strip events. There is a large difference in imaging quality between the two beam locations, with dramatic improvement in the strip boundary case. See Figure 7 for more discussion of the resolution achieved near strip boundaries with this method.

$$X = \frac{E_1 x_1 + E_2 x_2}{(E_1 + E_2)},\tag{1}$$

where E_1 , E_2 are the energies deposited in the two strips. The positions x_1 , x_2 were assigned within the strips registering those respective energies. The assignment of x_1 , x_2 was done via Gaussian probability distributions around the centers of each of the two strips. Charge shared event rate information was incorporated into that model by finding the percent of events that were single-strip, and then defining a single-strip event region as that percent of the total strip width. Half this width was used as the σ of the Gaussian probability distributions. In the single-strip case ($E_2 <$ threshold), the expression simplifies to assign the event to position x_1 .

The method in (11) took advantage of information gained from the relative magnitude of the two event energies in double-strip events for increased position information – on a population level, events with more even energy splits were placed closer to strip boundaries. However, the practice of randomly assigning x_1 , x_2 can lead to significantly different results for the same event each time position assignment is completed. Additionally, some double-strip events will be assigned to sub-strip locations far from the boundary between the two strips that registered. This is not in line with the behavior shown in 3.2, where almost all double-strip events occur near strip boundaries. Thus, it is desirable to develop a new method which utilizes energy ratios for their position information content, but which is informed by results from the ALS detector tests. We present such a method here.

3.3.1 Examining Energy Ratio Behavior

Through the ALS tests, we can investigate how energy is split between adjacent strips as a function of the beam position. We will begin this analysis by examining all data frames where the highest two energies recorded on a given side of the detector occurred in adjacent strips, expecting that this will include both true double-strip events, as well as single-strip events with adjacent noise signals (we will return to our threshold-based event selection method later on).

For every frame, we can define quantities related to the two event energies: the total energy E_{tot} , energy difference E_{diff} , and the energy ratio R_E . These are,

$$R_E = \frac{E_{\text{diff}}}{E_{\text{tot}}},\tag{2}$$

$$E_{\text{tot}} = E_1 + E_2,\tag{3}$$

$$E_{\text{diff}} = E_1 - E_2,\tag{4}$$

where $R_E = 0$ indicates an even split between the energies recorded in adjacent strips, while values of 1, -1 indicate all energy in one strip. We define the first strip (registering energy E_1) to be the lower-index strip (strips on each side of the detector being numbered 0-127). Finding R_E for every data frame, we examine the population of values at different beam positions. These R_E distributions in events with total energy between 17-24 keV are shown in Figure 6, calculated during the Pt-side (panels A-C) and Al-side (panels D-F) of the fine, L-shaped scan. Data losses during the Al-side scan can be seen again here (similar to in Figure 3).

Panels A and D show the R_E distributions over the entire scan, while panels B and E show a smaller segment, \sim 60 µm in width, which starts near one strip center, crosses the boundary, and ends near the center of the next strip over.

In all panels, two sets of horizontal lines define ranges in R_E associated with the primary and secondary thresholds: given the threshold values and the requirement for 17-24 keV total event energy, double-strip events with both components above 4 keV must necessarily lie within the two solid lines, while double-strip events with one component above 4 keV and one component above 1.4 keV must lie between the two dashed lines. Events with R_E values outside of the dashed lines may involve contributions from both photon-deposited charge and detector noise (noise contributions become significant below 1.4 keV).

Panels A and D show a consistent contribution of events appearing outside the dashed lines $(R_E \sim 1, -1)$, with bright, negatively-sloped features that span the entire range of R_E appearing at regular intervals. These

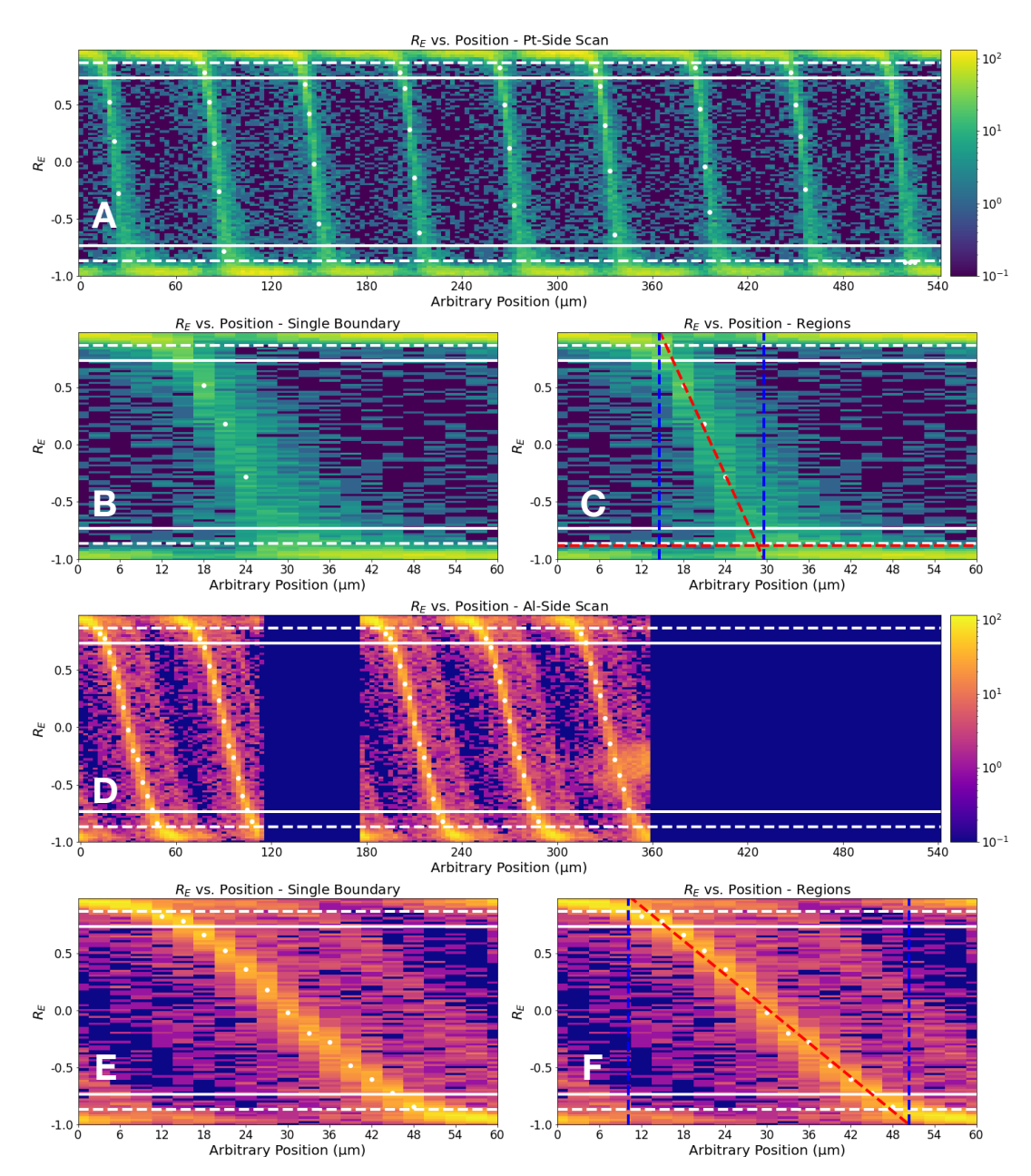


Figure 6. Distribution of ratios (R_E) between the top two highest energies recorded in each frame as a function of beam position. Plots include only events where the top two energies were recorded in adjacent strips, and the total energy is between 17-24 keV. Panels A-C show data taken during the L-scan branch orthogonal to Pt-side strips, while panels D-F show data taken during the branch orthogonal to the Al-side strips. Color bars shown next to panels A and D define color scale for all three plots associated with each of the two datasets. Panels A and D show the evolution of R_E over each full scan (see 3 for explanation of Al-side data losses). Panels B and E are subsets of the full scan, starting near the center of a strip, passing through a boundary, and halting near the center of the next strip over. White dots in some columns indicate the peaks of Gaussian fits to the R_E distribution at that position. Panels C, F show linear fits to the white dots (red dashed lines), characterizing the trends in R_E . Blue dashed lines mark the locations of intersections between these trends and $R_E = 1$, -1. R_E values above/below the white solid (dashed) lines indicate events which would be eliminated if the one- (two-) threshold event selection method was used to plot R_E for selected double-strip events only. Features in the edge regions above/below the dashed lines are expected to have a significant noise component.

features are true double-strip events, displaying the expected behavior of R_E near inter-strip boundaries: a position-dependent trend moving from highly uneven energy splits (large $|R_E|$) to more even splits ($R_E \sim 0$), and then back to uneven splits (large $|R_E|$ again).

Comparing with the strip boundary locations from 3.2, we confirm that the negatively sloped features occur at each strip boundary. We see (e.g. in Figure 6 A and D) that the slope and extent of these structures is similar at each strip crossing. This uniformity on each side leads us to assume that characterization of the strip boundaries seen here is likely a good description of the behavior across the detector.

To characterize the thin, negatively sloped structures at each boundary, we assume a linear relationship between R_E and incident photon position. The white dots shown over the data at certain positions in all panels of Figure 6 show the peaks of 1D Gaussian fits to the R_E profile at specific beam locations, quantitatively characterizing the structure.

In panels C and F, linear fits (red dashed lines) are shown to the white points. Additionally, the blue dashed lines highlight the positions at which the red fit line intersects with $(R_E = 1, -1)$. Thus, the region between the two blue lines at each strip boundary is the expected region (size: Al-side: 40 µm, Pt-side: 16 µm) in which incident events in this energy range will primarily register double-strip events.

Inversely, the region outside the two blue lines (including each strip center) can be expected to primarily host single-strip events. We therefore have again defined two sub-strip regions \P on each side of the detector, creating a geometry similar to that shown in Figure 4 in 3.2. However, we now have a great deal more information about the most likely incident position for each double-strip event: it may be finely determined within the double-strip event region via a linear relationship with R_E . Next, we will demonstrate a new imaging method using this information.

3.3.2 Implementing Energy-Ratio-Based Imaging

We outline a third method of imaging events in the *FOXSI* detectors, which will be called *energy ratio imaging*. Examples of this method are shown along with the others (strip-intersection-based imaging and zone-based imaging) in Figure 5. The procedure for assigning sub-strip positions to each recorded event in energy ratio imaging is as follows:

• **Double-strip Events**: For all recorded double-strip events, the energy ratio is computed via Equation 2. The location of the incident event (X) within the registered sharing region is estimated using the following expression:

$$X = B - R_E * M, (5)$$

where B is the location of the strip boundary, and M is the slope of the trend in R_E , estimated as presented in Figure 6.

• Single-strip Events: for single-strip events, a random position is assigned within the strip-center region outside the blue lines (dimensions: 20 µm on the Al-side, 44 µm on the Pt-side, centered around each strip center). We note that this is an approximation (as can be seen in Figure 3, a minority of single-strip events are observed in the regions near boundaries).

These instructions are one-dimensional; to perform 2D imaging as shown in Figure 5 they are completed for both the sides of the detector in each event. To further demonstrate the power of this imaging method, Figure 7 shows images at three adjacent beam positions near boundaries, along with a superposition of data at two beam positions 6 μ m apart. The two beam spots are clearly resolvable from each other, which (at the *FOXSI* sounding rocket focal length of 2 m) corresponds to resolving two small sources separated by only ~ 0.6 ".

[¶]The words "zone" and "region" are considered synonyms in their use in this chapter to describe smaller parts of each strip/strip intersection. To reduce confusion between the imaging approaches of sections 3.2 and 3.3, we refer to sub-strip "zones" in 3.2, and "regions" here.

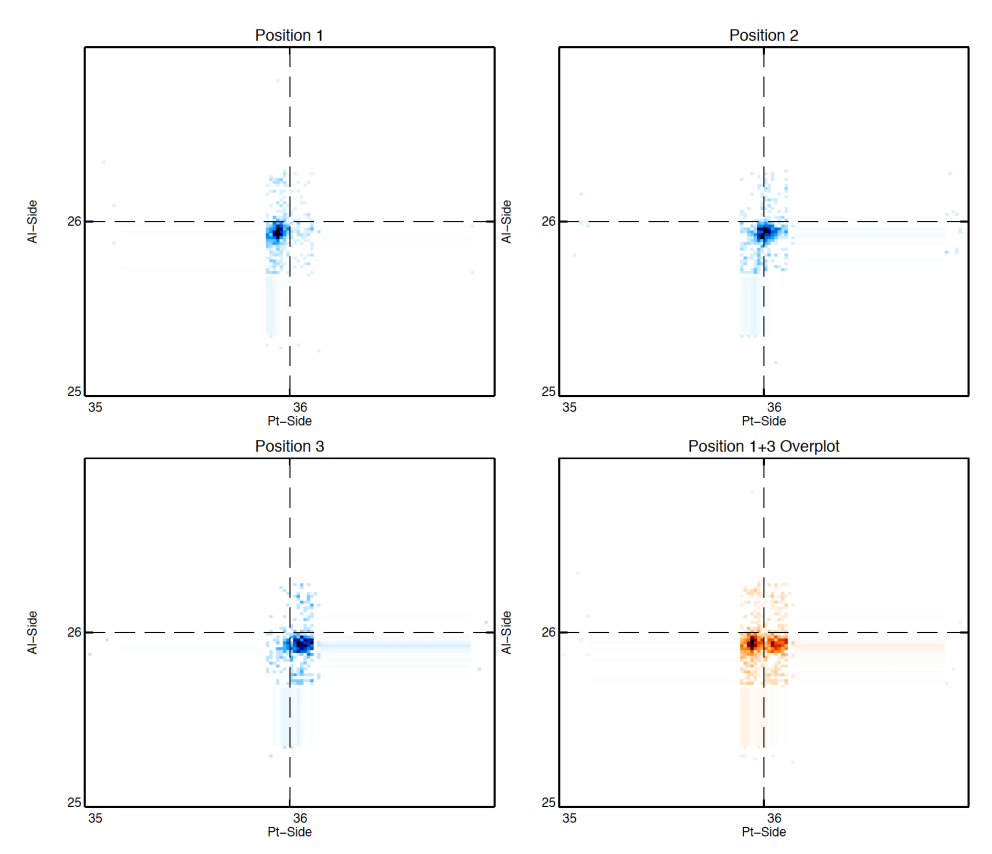


Figure 7. Images of the ALS beam at three adjacent positions in the fine, L-branch scan, all occurring near the boundaries between strips on both sides of the detector. Each image shows a very small section of the detector (two strip widths wide in each direction), with dashed lines indicating strip boundaries. 2D histograms of estimated incident photon locations have linear color scale. Positions 1-3 (top right and left, bottom right) are each 3 µm apart. The fourth panel shows data taken at positions 1 and 3 (beam 6 µm apart in total). Two distinct beam spots are clearly seen in the image, demonstrating the power of the energy ratio method to resolve small sources exceedingly close together.

Before moving to the next section (where a method similar to this is used as a component of a model of the response of the entire FOXSI instrument), we will first discuss the uncertainty in incident photon positions derived via this method. The uncertainty in single-strip event location is clear: such events could have occurred anywhere in the central region of the strip. The uncertainty in derived double-strip event locations is more complex, with two dominant components: the energy resolution of the detector, and uncertainty in the accuracy of the linear approximation to the R_E vs. position relationship.

The energy resolution of the *FOXSI* CdTe detectors at 21 keV is \sim 1 keV (FWHM of 21 keV peaks in single-strip spectra; similar values were found at other energies between 5-60 keV for FEC07 as reported in (16)). Because we are using energy information to calculate incident photon positions, the uncertainty in resulting position (δX) will depend on the energy resolution (δE). An explicit expression for this uncertainty is derived in (13), which finds,

$$\delta X = M \delta R_E = 2M \delta E \frac{\sqrt{E_1^2 + E_2^2}}{(E_1 + E_2)^2}.$$
 (6)

We see that δX is larger for smaller E_1, E_2 where the energy resolution is a relatively larger percent uncertainty in the energies. The maximum position uncertainty possible for a double-strip event found via the two-threshold method is ~ 6.5 µm corresponding to $E_1 = 1.4$ keV, $E_2 = 4$ keV (or the opposite). This is smaller than the sizes of the various regions, meaning that in the worst-case scenario (two near-threshold energies as components

of one incident photon) our ability to locate photons which caused double-strip events with this method is still slightly better than that of the zone-based imaging method described in 3.2. In all other cases, the uncertainty is smaller (for example, there is a <3 µm maximum uncertainty for events with 17-24 keV total energy, like all those in the example images in Figures 5 and 7).

The other possible source of uncertainty is connected to the linear approximation to the structure of near-boundary features in Figure 6. We see that there is some degree of deviation from the linear fit as shown in panels C and F, suggesting that this functional approximation fails to completely capture the dependence of R_E on beam position. To estimate the magnitude of the uncertainty which could be caused by this, we find the maximum distance of any one white peak point from the resulting linear fit on each side (δR_E). Using Equation 6 to convert these values to uncertainties in photon position, we find that this uncertainty is <3 µm on the Al side, and <1 µm on the Pt side. Thus this source of uncertainty is expected to have a similar (or lesser) effect than the uncertainty from energy resolution.

4. SIMULATING FOXSI RESPONSE

FOXSI images of solar HXR sources are influenced by the optics point spread function (PSF), the 2D segmentation of the detector into square strip intersections, and general noise in the detector readout. FOXSI images are also affected by the incidence of charge-sharing in the detector, as analyzed in Section 3. These properties each have a part in determining what FOXSI dataset will result from observing a given incident photon distribution.

By improving our understanding of these instrumental effects, we can improve our ability to extract a closer approximation of the original source. One strategy for achieving this is to create a model of the FOXSI instrument response. With a realistic model, generated sources can be convolved with the FOXSI system to simulate FOXSI data. Additionally, a corresponding deconvolution process can be used to extract a reconstructed incident source from the simulated data, and the original and reconstructed sources can be compared. Deconvolution processes which are successful in extracting incident simulated sources from modeled data represent strong candidates for implementation into standard practices for removing instrument response from real data.

This section will describe the generation and evaluation of a *FOXSI* response model and corresponding deconvolution process. It incorporates the measured PSF of a *FOXSI* optic, along with charge sharing properties extrapolated from detector tests at the ALS, as well as other measured/known detector properties. The incorporation of charge sharing into the modeled detector response means that the reconstructed source approximates the original to a higher degree of spatial resolution than what would result from using strip-based position knowledge only. In particular, we incorporate the energetics of charge sharing in a similar manner to the imaging method shown in 3.3.

4.1 Description of Model Framework

The response model developed is outlined in Figure 8, which shows the flow of information about a simulated (or hypothetical real) source through the different components of the *FOXSI* system to the point where data has been generated, and then back out to a reconstructed version of the incident distributions. This initial implementation was completed in one spatial dimension only, which, due to the strip-based readout, is equivalent to modeling behavior as it is read out on only one side of the detector. A full 2D implementation would be a natural extension of this work.

Step 1: Convolution with Optics PSF The PSF of several different FOXSI optics have been measured at the Stray Light Test Facility at MSFC (5). The PSF currently implemented is an approximation of measurements from optic X7, which flew on FOXSI-3 and was selected due to the intention (as of Fall 2021) of flying it also on FOXSI-4. The X7 measured PSF was found to be well-fit by a combination of three 2D Gaussian distributions, which together approximate the strong core and broader wings of the distribution. In order to implement the PSF in one spatial dimension, we took the average width (between the two directions) of each of the three Gaussian components, and summed the three distributions.

Convolution of the PSF with an input spatial distribution is done via simple matrix multiplication. This results in a post-optics spatial distribution which does not yet take into account the detector response. This can

Response Modeling Flowchart

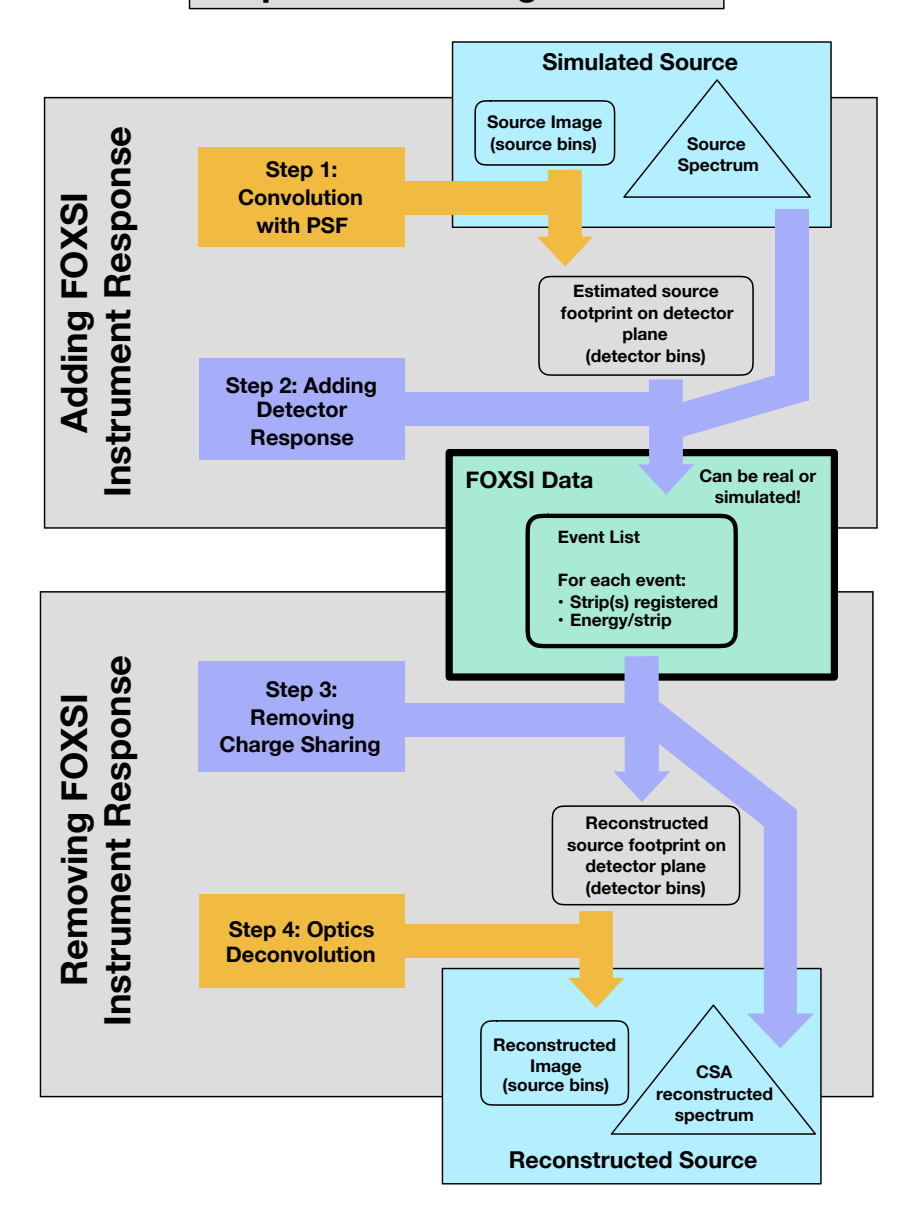


Figure 8. Flowchart showing process of modeling FOXSI instrument response. Inputs and outputs to each step (described in-text) are shown via the arrows in the diagram. The process is segmented into two parts: the top half starts with a simulated source, and results in simulated FOXSI data. The lower half starts with simulated FOXSI data and returns a reconstructed estimate of the simulated source. Methods used in this second process could also be applied to real FOXSI data, to attempt to better reconstruct an actual source.

be thought of as the source footprint on the detector plane. Note that, as can be observed in the flowchart (Step 1 of Figure 8), the optics convolution acts on the spatial distribution in isolation - an energy-dependent optics response has not been incorporated at this time.

Step 2: Adding Detector Response (Charge Sharing, Threshold, Energy Resolution) In order to add the response of the detector, we move from considering the simulated signal as a distribution into considering individual photon interactions. The post-optics spatial distribution and input source spectrum are combined to generate an event list (Step 2 of Figure 8). Each event in the list has both an incident position (X) and an energy (E), representing a photon about to interact with the detector, having passed through the optical path.

The incident position of each photon at this point in the process (X) is known to a finer degree of precision than the strip width. We check the location of X in relation to the detector strips, and follow one of two processes for applying detector response:

- If X falls in the central part of a strip (in the region where single-strip events are seen to dominate, as discussed in Section 3.3), the full energy E is assigned to the strip S_1 in which X is located ($E_1 = E$). After this, energy resolution is applied: gaussian noise is added to the value E_1 (1.2 keV FWHM, in agreement with the range of energy resolution values reported for FOXSI detector FEC07 in (16)). Finally, a "trigger threshold" is applied: if $E_1 < 4$ keV, the event is discarded.
- If X is close enough to a strip boundary to fall into the region where double strip events are dominant (again, see Section 3.3), the energy E will be split between two strips according to charge sharing rules. From X we find two strip values, S_1, S_2 , where S_1 is the strip in which X is located, and S_2 is the strip adjacent to S_1 which is closest to X. To figure out how much energy to assign to each strip, we solve the system of equations,

$$E = E_1 + E_2 \tag{7}$$

$$\frac{(E_1 - E_2)}{E} = \frac{(B - X)}{M} \tag{8}$$

where E_1, E_2 are the energies assigned to be deposited in S_1, S_2, B is the location of the boundary between S_1, S_2 , and M is the slope of the linear relationship between position and R_E , as found in Section 3.3. Note that Equation 8 is found by rearrangement of Equation 5. These can be solved for E_1, E_2 , resulting in the expressions:

$$E_1 = \frac{E}{2} \left[1 + \frac{B - X}{M} \right] \tag{9}$$

$$E_2 = \frac{E}{2} \left[1 - \frac{B - X}{M} \right]. \tag{10}$$

After assigning energies to the two relevant strips, energy resolution is applied in the same manner as in single-strip events above. Finally, a detector threshold is applied: first, a trigger threshold (4 keV) is used to determine if an event will be recorded (one of the two values E_1 , E_2 must be >4 keV). Then, a secondary threshold (1.4 keV) is used to check if the second energy is above that lower value (if not, the secondary event is discarded). This means that an incident photon in the boundary regions can generate signals in anywhere from 0-2 strips, depending on the resulting values of E_1 , E_2 .

After all of the above is complete, a simulated *FOXSI* dataset has been generated. To distinguish from the use of "event list" above, this will be referred to as a "frame list", wherein all signals generated by one "event" or simulated photon are reported together as one *FOXSI* data frame. The frame list is an analogue for the format of real *FOXSI* data, and contains no more or less information about the incident simulated source than real data contains about the physical source of the observed emission. Note that we have not incorporated coincidence events (where more than one photon interacts in the detector during a single frame) in this model.

Step 3: Removing Charge Sharing The effects of energy resolution and the detector threshold represent a fundamental loss of information about the source distribution. However, inversion of the charge sharing process is possible. For each frame in the frame list which has registered at least one strip above the threshold, we implement a reconstruction process using the strip numbers and registered energies (Step 3 of Figure 8). This is the energy-ratio-based imaging method described in 3.3.

Removing charge sharing in this manner results in a population of event locations, the distribution of which is treated as a reconstruction of the source footprint on the detector plane. To reconstruct the initial incident spectrum, we sum the energies in each frame (CSA), including the sub-threshold energies added back to some single strip events during the imaging method.

Step 4: Optics Deconvolution In order to estimate the true source spatial distribution from the reconstructed source footprint on the detector plane, we desire to remove (or reduce) the influence of the optics on the distribution (Step 4 of Figure 8). To do this, a common deconvolution method is employed: Richardson-Lucy deconvolution, a maximum likelihood estimation (MLE) process named after two researchers who each developed it independently (17; 18).

There are many "off-the-shelf" implementations of MLE deconvolution following the Richardson-Lucy method. For this project, a custom 1D implementation was developed in IDL which allows for the source and observed arrays to be different sizes. This is helpful when pursuing sub-strip resolution, when new advances in understanding of sub-strip spatial properties can motivate increasingly small bin sizes in the observed array.

The mathematical structure of the deconvolution process is described in (13), following the logic of (17). It is implemented with the requirement to input a "guess" for the source distribution (often, a uniform distribution is used), in addition to the PSF and the reconstructed source footprint on the detector plane. The number of deconvolution iterations must also be chosen. As can be seen in Section 4.2, the ideal number of deconvolution iterations depends on the source distribution.

4.2 Examples with Simulated Sources

Both Figures 9 and 10 show the different spatial distributions resulting at different stages of the process of taking a simulated 1D source, applying the *FOXSI* response, and then reconstructing an approximation of the incident source despite information lost during the response process. In both input spatial distributions there are two peaks spaced one strip width apart; in Figure 9 each source peak is at a strip center and in Figure 10 each source peak is at a strip edge. Figure 11 shows the corresponding spectra at three stages of the process. Only one set of example spectra are shown for the two example spatial distributions because changing the location of the peaks was not seen to have a noticeable effect on the spectral evolution between these two cases. The following list effectively provides captions for each panel in these figures (panels A-E in 9 and 10 and corresponding panels in Figure 11).

- A. The first panels of Figures 9 and 10 show the input simulated source, consisting of two Gaussian peaks over a flat continuum. The Gaussians have FWHM corresponding to ~15 and ~30 µm, respectively, or around 1.5" and 3". The continuum is at about 30% of the magnitude of the smaller peak, and was added due to the common situation of bright solar HXR sources (flares, etc.) appearing in the presence of dimmer, more diffuse emission from surrounding active regions. The first panel of Figure 11 shows the corresponding input spectral distribution, which is meant to replicate the incident ALS beam component used for the analysis in 3.
- **B.** The second panels in Figures 9 and 10 show the source footprint on the detector plane, after convolving the input with the optics PSF (Step 1, as shown in Figure 8 and discussed in 4.1). The PSF acts to "smear out" the spatial source map. The red line shows the original incident source, for comparison.
- C. The third panels in Figures 9 and 10 show the strip-binned image, equivalent to the 2D strip images shown in the top panels of Figure 5. In both cases (Figures 9 and 10) the strip-binned image fails to resolve the two sources, as they are located only one strip pitch apart. The second panel of Figure 11 shows the

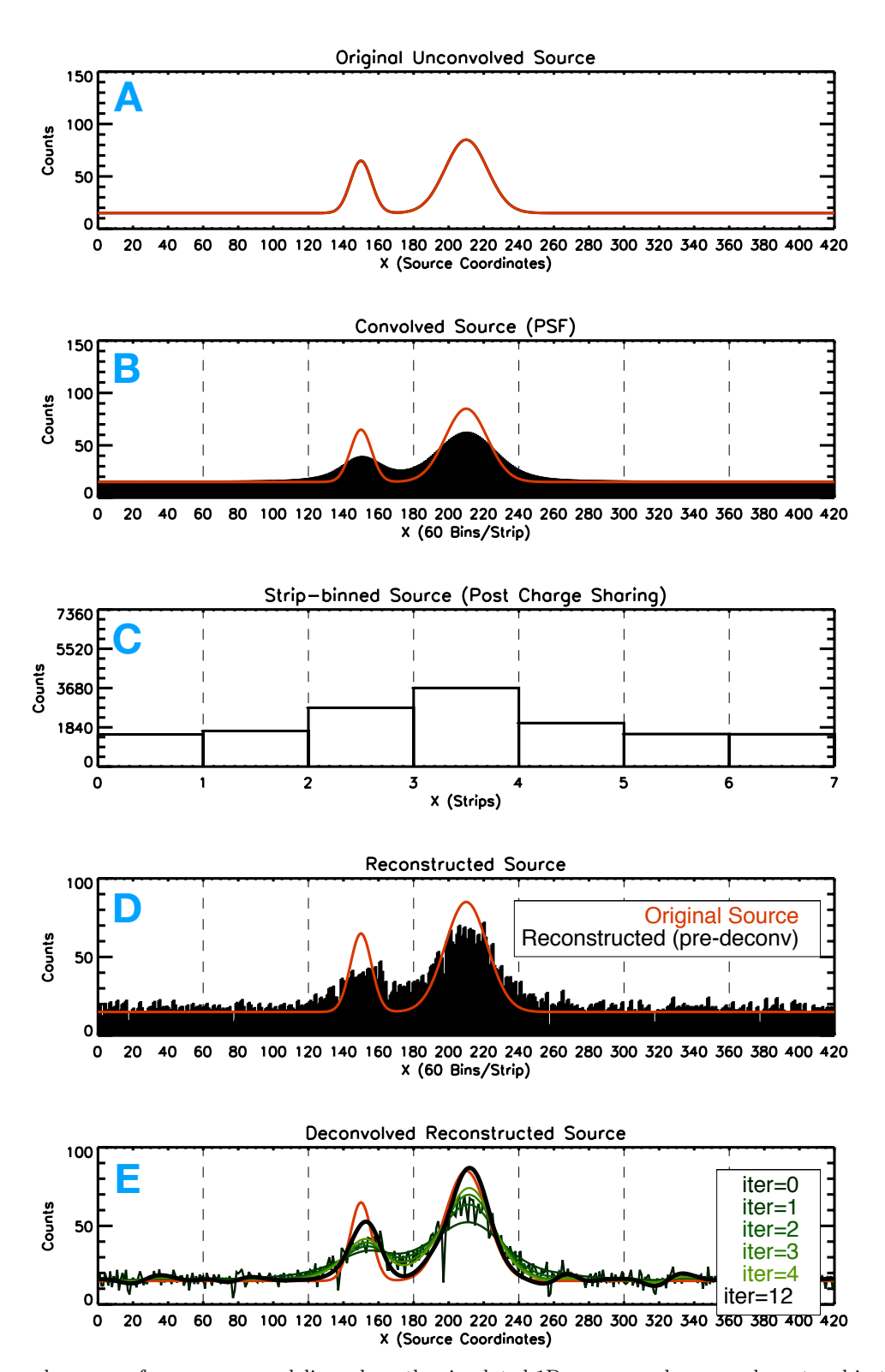


Figure 9. Example process for response modeling where the simulated 1D source peaks are each centered in the middle of a detector strip. Details of each panel (for this and other examples) are described in-text in 4.2.

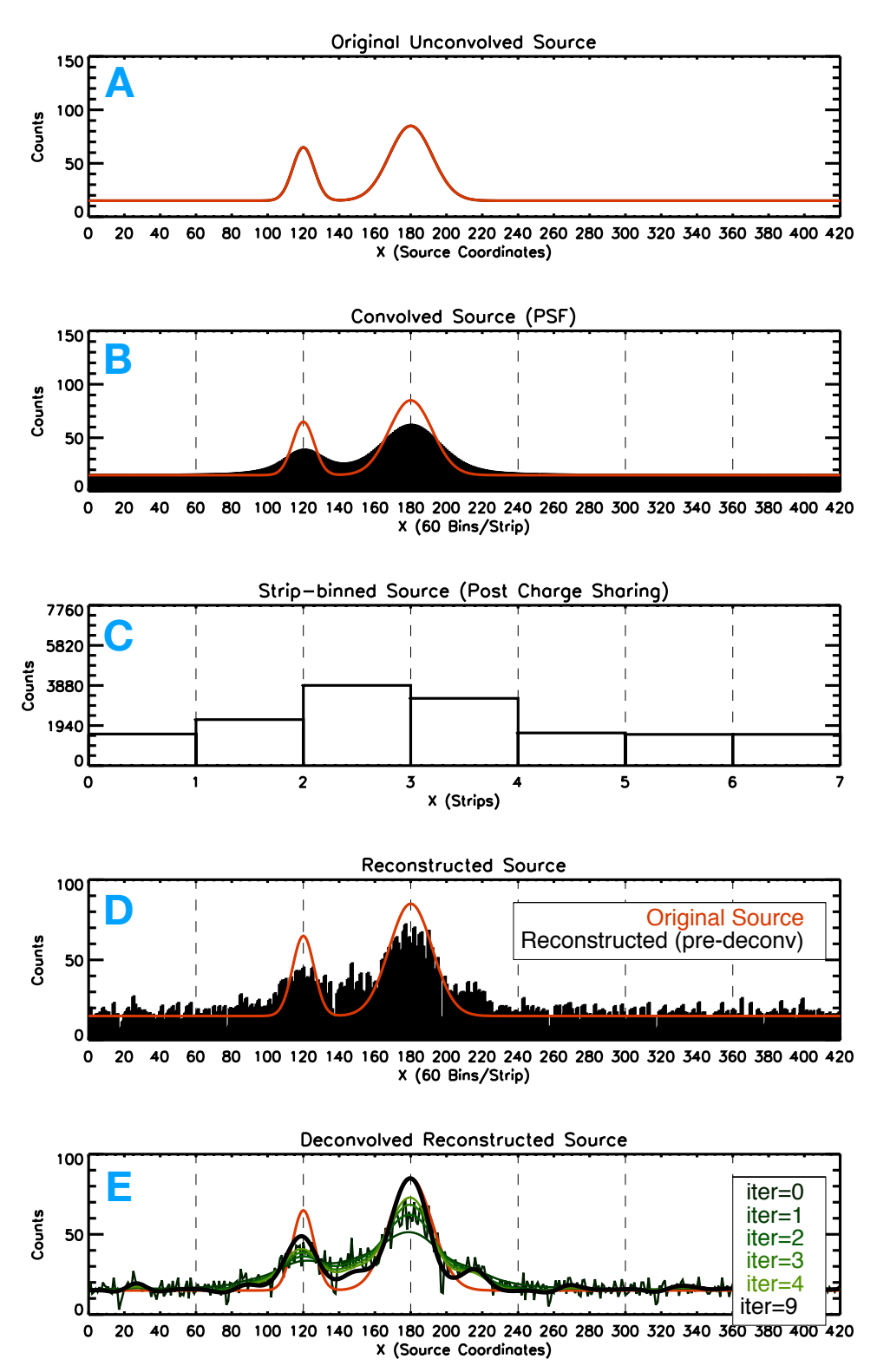


Figure 10. Example process for response modeling where the simulated 1D source peaks are each centered at the edge of a detector strip. Details of each panel (for this and other examples) are described in-text in 4.2.

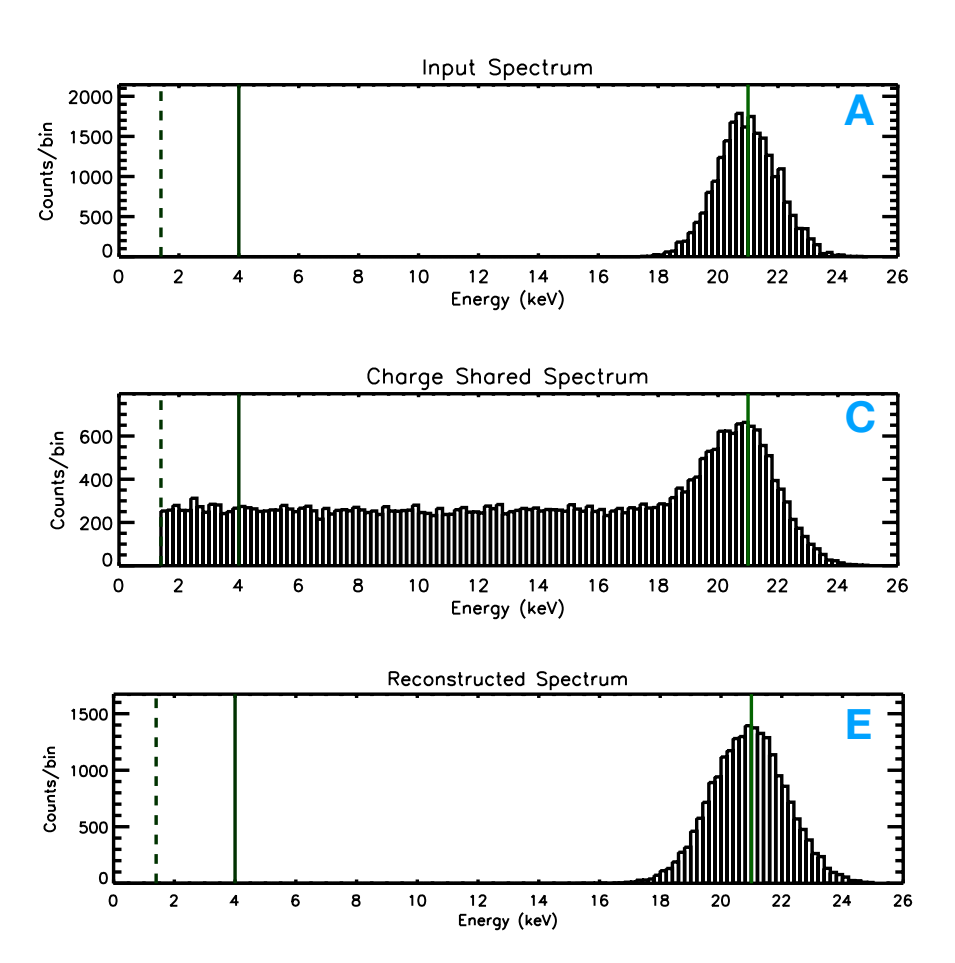


Figure 11. Example spectra corresponding to three panels of Figures 9 and 10. Details of each panel (for this and other examples) are described in-text in 4.2.

predicted raw spectrum recorded in the FOXSI detector. The spectral peak around 21 keV is reduced, and many lower-energy events are seen (due to charge sharing splitting incident energies into components). This stage of the process represents FOXSI data, and has been achieved by applying Step 2 as outlined in Figure 8 and discussed in 4.1.

- **D.** The fourth panels of Figures 9 and 10 are the reconstructed source footprints on the detector plane, after the removal of charge sharing effects (as described in Step 3 of Figure 8 and 4.1). The red lines again show the original incident source, for comparison.
- E. The fifth panels of Figures 9 and 10 show the final reconstructed source, after deconvolution (Step 4 of Figure 8 and 4.1). The red line again shows the original incident source, for comparison. Different deconvolution intervals are shown in varying shades of green, with the best result shown as a thicker black line. The determination of the best result is done by cross-correlating the initial input source with the deconvolved result at each stage, resulting in slightly different numbers of iterations between the two examples. This is an obviously unfeasible stopping condition in a real-data case, making development of an input-independent stopping condition a necessary aspect of incorporating this type of reconstruction into analysis of real data. The third and final panel of Figure 11 shows a reconstructed spectrum (via CSA). The process has broadened the spectral peak at 21 keV, as would be expected with the application of energy resolution and uncertainty gained from reconstructing below-threshold events.

In both examples (Figures 9 and 10) it is clear that we resolve the presence of more than one source, despite

Example	Peak Widths	Peak Locations	Peak Amplitude	Greatest Artifact
	(% of input peak)	(displacement)	(% of input peak)	Peak Amplitude ¹
Center Peaks	Peak 1: 144%	Peak 1: 2.3 μm	Peak 1: 75%	13%
(Figure 9)	Peak 2: 96%	Peak 2: 1.8 μm	Peak 2: 103%	
Edge Peaks	Peak 1: 149%	Peak 1: 1.1 μm	Peak 1: 67%	37%
(Figure 10)	Peak 2: 87%	Peak 2: 0.7 μm	Peak 2: 101%	

¹ Artifact peak amplitude reported as a percent of the amplitude of the fainter reconstructed peak.

Table 2. Quantitative comparison between the input simulated sources and resulting reconstructed distributions as seen in Figures 9 and 10, found after subtracting the input continuum. Source peaks are labeled from left to right as seen in the figures (i.e. Peak 1 is the fainter peak in both cases).

their sub-strip size. For a more quantitative evaluation of the performance achieved, Table 2 reports parameters from Gaussian fits to the three brightest peaks observed in the reconstructed distributions – the two reconstructed peaks, and the highest-amplitude artifact of the reconstruction.

We observe a high-quality reconstruction of the input, with locations of the peaks found within a few µm of their input locations (all found to be displaced by under 4% of the strip pitch in comparison to the input peak locations). For the brighter of the two peaks in each example, we even reconstruct a close approximation of the peak shape (width within 87% and amplitude nearly identical). The fainter peaks in the reconstructed arrays are shortened and broadened in relation to the corresponding input source peaks, but are still well-located and distinguishable from their neighbors.

The artifact peak heights—reaching 37% of the height of the fainter source peak in one case—motivate future work in achieving a robust stopping condition for the deconvolution process, which otherwise may magnify such features until they are indistinguishable from observed sources. In total, we are encouraged by the performance demonstrated, which suggests that the charge-sharing-driven increases in detector resolution we have achieved are carried forward to whole-instrument improvements in resolution, despite the influence of the PSF.

5. CONCLUSIONS AND NOTES ON IMPLEMENTING NEW METHODS

In this paper, we have developed and evaluated new methods for imaging with FOXSI-3 detectors, informed by detailed measurements of charge shared events taken at an ALS X-ray beamline. We first analyzed properties of charge shared events from a 21 keV component of a beam illuminating a FOXSI CdTe detector, and used those properties to develop imaging methods which increase the spatial resolution of the system. In particular, Figures 5 and 7 show the power of one of the methods developed (energy ratio imaging) to locate small, sub-strip-sized sources observed by the FOXSI detectors when they occur in certain regions. With this method, we have resolved two sources 6 μ m (in the FOXSI rocket context, 0.6") apart, an order of magnitude better than the intended design of the detector.

This level of precision is only available in certain parts of detector strips, forming a grid of regions where extremely high resolution imaging can be achieved. Such a strong spatial dependence in the resolution of these detectors may motivate an observing strategy wherein some form of pointing jitter or controlled translation is used to bring *all* portions of an observed source into the high-resolution regions over the course of a certain observation interval, somewhat akin to raster methods used by slit-based spectrographs to build up spatial maps over time.

However, we note that even without implementing such a strategy our charge-sharing-informed methods have still improved our our ability to locate incident sources regardless of position. We achieve at least \sim 3" resolution everywhere on the detector, improving over the \sim 6" pitch of the strips (all values in arcseconds refer to equivalent resolution at a 2 m sounding rocket focal length).

Additionally, via a response modeling process, we showed that even when combined with the simulated effects of previous-generation (FOXSI-3) optics, this increased detector resolution still translated to increased resolution

of the entire FOXSI instrument. Two simulated sources placed only one strip-width apart were easily identified in the reconstructed spatial distribution, and even located to within a few μ m of the input source locations.

The work completed here looked specifically at 21 keV incident photons, as the scan used here (7 keV, 21 keV, 28 keV) is the only available dataset with a fine enough step size to do this characterization (and the population of charge shared 7 keV events is reduced by the 4 keV trigger threshold). We know that the portion of events which charge share is energy dependent (e.g. 9), with more charge shared events from higher-energy photons. Thus, the relationships we have found between energy ratio and photon position at 21 keV may not be valid for describing events at lower total energies.

This project could be expanded through further ALS (or similar) tests using beams at other energies: scans with the same step size and beam size should be completed at beam energies across the *FOXSI* charge shared event energy range (~8-20 keV, given the 4 keV threshold). The uniformity we have seen between strips in this analysis makes it a reasonable plan to take significantly shorter scans (covering just a few strips in each direction) in order to repeat this analysis at more energies in a time-efficient manner. If this type of testing is not possible, the variable full-detector charge shared event rates as a function of energy (e.g. from sealed source illuminations) could be measured and used to extrapolate to different energy-ratio vs. position relationships at different ranges in incident photon energy.

We additionally note that while charge sharing is expected to occur similarly in FOXSI-4 detectors, the specific model parameters found using FOXSI-3 detector measurements are not necessarily directly applicable to the FOXSI-4 system (7; 10). Thus, a further area of future work is to make similar measurements with FOXSI-4 detectors, use them to customize these imaging methods, and then evaluate the new expected performance using the response modeling process.

Looking farther into the future, we note that the imaging methods developed here could additionally be used with other similar segmented detector systems wherever increased spatial resolution is desirable. The imaging results achieved through charge sharing knowledge gained via tests of the FOXSI-3 detectors at the ALS provides a clear demonstration of the power of detector characterization using fine beam scans. Such tests have the potential to achieve similar results for any segmented system in which charge shared events are observed. One obvious implementation would be in a detector designed for use in a space-based solar-dedicated instrument using the heritage of the FOXSI rocket program.

ACKNOWLEDGMENTS

This work was supported under the 2019 NASA Fellowship Program (80NSSC19k1687). The FOXSI sounding rocket experiment is funded by NASA grants 80NSSC21K0030, 80NSSC17K0430, NNX08AH42G, NNX11AB75G, and NNX16AL60G. The Univeristy of Minnesota team is supported by an NSF Faculty Development Grant (AGS-1429512), an NSF CAREER award (NSF-AGS-1752268), and the SolFER DRIVE center (80NSSC20K0627). This work was also supported by JSPS KAKENHI Grant Numbers 22J12583, 21H04486, 18H05463, and 24244021. S.N. is also supported by FoPM (WINGS Program) and the JSR Fellowship (University of Tokyo, Japan).

This research used resources of the Advanced Light Source, which is a DOE Office of Science User Facility under contract no. DE-AC02-05CH11231.

References

- [1] Benz, A. O., "Flare observations," Living Rev. Sol. Phys. 14(1), 2 (2016).
- [2] Krucker, S. and Lin, R. P., "Hard X-Ray Emissions from Partially Occulted Solar Flares," ApJ 673, 1181–1187 (Feb. 2008).
- [3] Lin, R. P., Dennis, B. R., Hurford, G. J., Smith, D. M., Zehnder, A., Harvey, P. R., Curtis, D. W., Pankow, D., Turin, P., Bester, M., Csillaghy, A., Lewis, M., Madden, N., van Beek, H. F., Appleby, M., Raudorf, T., McTiernan, J., Ramaty, R., Schmahl, E., Schwartz, R., Krucker, S., Abiad, R., Quinn, T., Berg, P., Hashii, M., Sterling, R., Jackson, R., Pratt, R., Campbell, R. D., Malone, D., Landis, D., Barrington-Leigh, C. P., Slassi-Sennou, S., Cork, C., Clark, D., Amato, D., Orwig, L., Boyle, R., Banks, I. S., Shirey, K.,

- Tolbert, A. K., Zarro, D., Snow, F., Thomsen, K., Henneck, R., McHedlishvili, A., Ming, P., Fivian, M., Jordan, J., Wanner, R., Crubb, J., Preble, J., Matranga, M., Benz, A., Hudson, H., Canfield, R. C., Holman, G. D., Crannell, C., Kosugi, T., Emslie, A. G., Vilmer, N., Brown, J. C., Johns-Krull, C., Aschwanden, M., Metcalf, T., and Conway, A., "The Reuven Ramaty High-Energy Solar Spectroscopic Imager (RHESSI)," Sol. Phys. 210, 3–32 (Nov. 2002).
- [4] Glesener, L., Krucker, S., Christe, S., Ishikawa, S.-n., Buitrago-Casas, J. C., Ramsey, B., Gubarev, M., Takahashi, T., Watanabe, S., Takeda, S., Courtade, S., Turin, P., Mcbride, S., Shourt, V., Hoberman, J., Foster, N., and Vievering, J., "The foxsi solar sounding rocket campaigns," in [Space Telescopes and Instrumentation 2016: Ultraviolet to Gamma Ray], 99050D (07 2016).
- [5] Christe, S., Glesener, L., Buitrago-Casas, C., Ishikawa, S.-N., Ramsey, B., Gubarev, M., Kilaru, K., Kolodziejczak, J. J., Watanabe, S., Takahashi, T., Tajima, H., Turin, P., Shourt, V., Foster, N., and Krucker, S., "Foxsi-2: Upgrades of the focusing optics x-ray solar imager for its second flight," *Journal of Astronomical Instrumentation* 05(01), 1640005 (2016).
- [6] Musset, S., Buitrago-Casas, J. C., Glesener, L., Bongiorno, S., Courtade, S., Athiray, P. S., Vievering, J., nosuke Ishikawa, S., Narukage, N., Furukawa, K., Ryan, D., Dalton, G., Turin, Z., Davis, L., Takahashi, T., Watanabe, S., Mitsuishi, I., Hagino, K., Kawate, T., Turin, P., Christe, S., Ramsey, B., and Krucker, S., "Ghost-ray reduction and early results from the third FOXSI sounding rocket flight," in [UV, X-Ray, and Gamma-Ray Space Instrumentation for Astronomy XXI], Siegmund, O. H., ed., 11118, 321 336, International Society for Optics and Photonics, SPIE (2019).
- [7] Buitrago-Casas, J. C., Vievering, J., Musset, S., Glesener, L., Athiray, P. S., Baumgartner, W., Bongiorno, S., Champey, P., Christe, S., Courtade, S., Dalton, G., Duncan, J., Gilchrist, K., Ishikawa, S.-n., Jhabvala, C., Kanniainen, H., Krucker, S., Gregory, K., Martinez Oliveros, J. C., McCracken, J., Mitsuishi, I., Narukage, N., Pantazides, A., Peretz, E., Perez-Piel, S., Ramanayaka, A., Ramsey, B., Ryan, D., Savage, S., Takahashi, T., Watanabe, S., Winebarger, A., and Zhang, Y., "FOXSI-4: the high resolution focusing X-ray rocket payload to observe a solar flare," in [Society of Photo-Optical Instrumentation Engineers (SPIE) Conference Series], Society of Photo-Optical Instrumentation Engineers (SPIE) Conference Series 11821, 118210L (Aug. 2021).
- [8] Ishikawa, S.-n., Katsuragawa, M., Watanabe, S., Uchida, Y., Takeda, S., Takahashi, T., Saito, S., Glesener, L., Buitrago-Casas, J. C., Krucker, S., and Christe, S., "Fine-pitch cdte detector for hard x-ray imaging and spectroscopy of the sun with the foxsi rocket experiment: Fine-pitch cdte hard x-ray detector," *Journal of Geophysical Research: Space Physics* (07 2016).
- [9] Furukawa, K., Buitrago-Casas, J., Vievering, J., Hagino, K., Glesener, L., Athiray, P., Krucker, S., Watanabe, S., Takeda, S., Ishikawa, S., Musset, S., Christe, S., and Takahashi, T., "Development of 60μm pitch cdte double-sided strip detectors for the foxsi-3 sounding rocket experiment," Nuclear Instruments and Methods in Physics Research, Section A: Accelerators, Spectrometers, Detectors and Associated Equipment 924, 321–326 (Apr. 2019).
- [10] Nagasawa, S., "Imaging and spectral performance of wide-gap CdTe double-sided strip detectors for FOXSI-4 sounding rocket experiment," in [9th Conference on New Developments in Photodetection], New Developments in Photodetection (in prep.).
- [11] Furukawa, K., Nagasawa, S., Glesener, L., Katsuragawa, M., Takeda, S., Watanabe, S., and Takahashi, T., "Imaging and spectral performance of a 60μm pitch cdte double-sided strip detector," Nuclear Instruments and Methods in Physics Research Section A: Accelerators, Spectrometers, Detectors and Associated Equipment 978, 164378 (2020).
- [12] Robinson, A. and Schlachter, A., "The als—a third-generation light source," Nuclear Instruments and Methods in Physics Research Section A: Accelerators, Spectrometers, Detectors and Associated Equipment 291(1), 499–504 (1990).

- [13] Duncan, J. M., Energy Release in Solar Microflares and New Methods for X-ray Imaging Spectroscopy, PhD thesis, University of Minnesota (July 2022).
- [14] Glesener, L. E., Faint Coronal Hard X-rays From Accelerated Electrons in Solar Flares, PhD thesis, University of California, Berkeley (Jan. 2012).
- [15] Duncan, J. and Glesener, L., "Foxsi detector data from 2018-2019 advanced light source experiments," (June 2022).
- [16] Vievering, J. T., Nature of Energy Release and Transfer for Solar and Stellar Flares Using High-sensitivity Hard X-ray Instrumentation, PhD thesis, University of Minnesota (Jan. 2019).
- [17] Lucy, L. B., "An iterative technique for the rectification of observed distributions," AJ 79, 745 (June 1974).
- [18] Richardson, W. H., "Bayesian-based iterative method of image restoration," J. Opt. Soc. Am. 62, 55–59 (Jan 1972).